ARTICLE

Synthesis by Spray Pyrolysis of Mesoporous $NbRu_yO_z$ as Electrocatalyst Supports in Fuel Cells

Daniel A. Konopka,* Svitlana Pylypenko, Plamen Atanassov, and Timothy L. Ward*

Department of Chemical and Nuclear Engineering, University of New Mexico, 209 Farris Engineering Center, Albuquerque, New Mexico 87131

ABSTRACT In this study, spray pyrolysis was used to produce two mesoporous powders, niobium oxide and niobium oxide with 12% ruthenium (by weight, metal basis, based on precursor mixture), as potential catalytic supports in fuel cells. Niobium oxide and ruthenium-modified niobium oxide powders displayed spherical particle morphology with internal mesoporosity introduced by surfactant templating, providing surface areas as high as 183 and 167 m^2/g, respectively, after postprocessing that included an acid etch and calcination. The incorporation of ruthenium into niobium oxide, coupled with appropriate postsynthesis treatment, resulted in a material with electrical resistance that was reduced by roughly 5 orders of magnitude relative to unmodified niobium oxide. The structure and properties of these two materials subject to different postprocessing treatments were extensively characterized, and dynamic factors related to aerosol and subsequent thermal processing of these materials are discussed. Cyclic voltammetry showed that the ruthenium-modified material possessed activity for methanol oxidation in a basic environment.

KEYWORDS: aerosol synthesis • spray pyrolysis • structured metal oxides • conductive oxides • electrocatalyst supports • fuel cell materials • niobium oxide

1. INTRODUCTION

Fuel cell research has largely been dominated by discussion of possible ways to utilize evermore expensive platinum electrocatalysts. In H_2- or alcohol-based fuel cells, where hydrogen is the ultimate electron source, platinum remains the definitive performer. At the anode, the current state of the art utilizes decorated nanoparticles of PtRu alloy phase supported on high-surface-area carbon blacks (1). It is generally believed that the improved fuel oxidation and enhanced resistance to CO poisoning seen with PtRu is a result of the bifunctionality of the material (2, 3).

Carbon blacks have traditionally been used as the catalytic support for PtRu due to their excellent electronic conductivity and high surface areas ranging from 150 to 1200 m^2/g. The outer surface of the most commonly used carbons is graphitic with a low degree of oxidation, whereas the interior remains amorphous and especially susceptible to corrosion (4, 5). There are three primary means of failure of carbon as a catalytic support. The first develops from percolation effects in the conductive carbon matrix as the material shifts and its simple morphology is unable to maintain as many points of electrical contact among particles, resulting in ohmic losses. Because carbon does not interact with the catalyst, kinetic losses also occur when platinum particles agglomerate and migrate around and off of the support surface, leading to sintering and loss of catalyst/support contact. Consequently, platinum and ruthenium have been shown to detach from the carbon and migrate across the ion exchange membrane (6−8). Finally, carbon forms surface oxides that create a hydrophilic interface and lead to flooding of the support, ultimately hindering fuel flow to the catalyst.

Carbon supports do not participate in the catalytic oxidation/reduction reactions and offer low stability, leading to degradation of the fuel cell. For these reasons, noncarbon supports are being explored as an alternative. Transition metal oxides possessing variable oxidation states are one class of noncarbon material that offers promise as electrocatalyst supports because of the generally superior stability, and reasonable electrical conductivity associated with substoichiometric oxides. This class of materials for electrocatalyst supports has been recently reviewed (9). One challenge with these materials is the need for the oxide to be partially reduced to provide electronic conductivity while maintaining high surface area (10). In some cases, incorporating a second oxide element, such as Nb into titanium oxide (11, 12), can enhance electronic conductivity. Alternatively, small to moderate weight percents of metal oxides supported on carbon have also been implemented as pseudosupports for catalyst (2, 13).

Niobium oxide, when modified to enhance electrical conductivity, is one of several potentially suitable materials for replacing carbon as a catalytic support in membrane fuel cells (11, 14). Literature has shown that niobia can play a complementary role in the catalysis of oxygen reduction (12, 13), hydrogen oxidation (15), and methanol oxidation (2, 11), wherein Pt activity is enhanced depending upon the form and quantity of the metal oxide. The design require-

* Corresponding author. Phone: (505) 277-2067. Fax: (505) 277-5433. E-mail: tlward@unm.edu.

Received for review September 3, 2009 and accepted December 5, 2009

DOI: 10.1021/am900601q

Published on Web 12/16/2009

ments of alternative electrocatalyst support materials are rigorous. A competitive replacement must have a reasonably high surface area, exhibit a degree of catalyst stabilization, have minimal gas transport resistance, be electrically conductive, and have the proper balance of hydrophobic surface chemistry so as to avoid inhibiting levels of hydration.

Spray pyrolysis (SP) is a versatile synthetic approach capable of producing spherical mesoporous oxide particles that, when incorporated into a well-engineered electrode architecture, could provide an attractive electrocatalyst support system. In particular, SP is well-suited to effectively utilize evaporation induced self-assembly (EISA) of amphiphilic templates to synthesize mesoporous materials with controlled pore size and mesostructure and relatively high internal surface area (16−18). The purity, composition, and uniformity of precursor solutions for SP are highly controllable, and that control is also reflected in the properties of aerosol droplets produced from the solution (19, 20). Each droplet within such an aerosol can be viewed as an independent microreactor with homogeneously mixed components and minimal internal diffusion resistance (21). Total reaction time is relatively short in SP reactor systems, usually in the range of seconds or tens of seconds. SP also has excellent potential as a scalable process.

Here we report on the use of spray pyrolysis to produce mesoporous niobium oxide and ruthenium-modified niobium oxide materials as potential catalytic supports in fuel cells. Niobium oxide is compared to niobium oxide modified with ruthenium. Varying post-treatments followed by characterization and analysis reveal that spray pyrolysis with appropriate postprocessing can produce oxide materials with desirable properties as fuel cell electrocatalyst supports.

2. EXPERIMENTAL SECTION

2.1. Precursor Materials. $NbCl_5$ powder was acquired from Sigma-Aldrich, $RuCl_3$ from Fischer Scientific, and Pluronic-123 (nonionic triblock copolymer) from BASF. All materials were used as received. In the synthesis of mesoporous NbO_x, 1 g of P123 was dissolved in 10 g of ethanol. Added to this was 2.6 g of $NbCl_5$, after which the entire mixture was stirred for 10 min until all $NbCl_5$ was dissolved, yielding a transparent solution. A similar niobium material doped with 12% Ru by weight of metals, hereafter referred to as $NbRu_yO_z$, was prepared by including 1 g of H_2O and 0.385 g $RuCl_3$ after 22 g ethanol, 2 g P123, and 3.70 g $NbCl_5$. The small amount of additional water was necessary to thoroughly dissolve the $RuCl_3$ into solution.

2.2. Spray Pyrolysis Apparatus and Materials Synthesis. Three separate sections comprise the spray pyrolysis apparatus. A TSI Inc. aerosol generator (Model 3076) utilizes a single inert gas inlet to atomize the precursor solution, producing aerosolized liquid precursor droplets. A three-zone horizontal furnace spanned by a 3 in. outer diameter mullite tube from Coorstek, into which the aerosol stream feeds, is responsible for drying and thermal decomposition of the droplet material. The three-zone horizontal furnace with an effective heated length of 3 ft was set to provide a 200 °C temperature profile, determined by thermocouple measurement at sequential points inside the tube. Precursor solutions were fed into the aerosol generator from an Ehrlenmeyer flask and carried through the tube as an aerosol using N_2 carrier gas at 1.5 SLM (standard liters per minute). Collection was achieved with a porous membrane filter (HT-Tuffryn 450 Disk Filter, 0.20 μm pore size) to separate the dried material from the gas stream. The filter temperature was maintained at approximately 100 °C to prevent water condensation.

2.3. Post-Treatment of Aerosol-Derived Materials. Once cooled to room temperature, powders were immediately collected off the filter paper. The bulk sample was divided into several smaller groups. Post-treatment given to samples containing only niobia is similar to what has previously been reported in literature for templated Nb_2O_5 via sol−gel synthesis (14, 16, 18, 22−24). This involved an acid wash in excess 0.3 M H_2SO_4 solution followed by a water rinse, and then drying in ambient air and calcination in air (ramp at 10 °C/min to 400 °C, then held for 4 h). Separate cases in the literature show acid washing and calcination to each be effective in the removal of amphiphilic surfactants, including P123 (18, 25). In our case, both were necessary to fully expose the interior mesoporosity of the material.

Post-treatment steps of samples containing ruthenium were somewhat altered compared to pure niobium oxide. The acid washing step was carried out in various degrees, including omission, to determine its true benefit. Samples are named first according to the parent sample from the filter paper, the degree of washing received, and finally the heating process. For example, NbO_x-Dry-Air, contained no Ru, received no acid wash and was calcined in air. $NbRu_yO_z$-Wet-N_2/H_2, initially contained 1:8 Ru to Nb (or 12 wt %), received only enough acid wash solution as to be wetted, and was reduced under N_2/H_2 atmosphere. For materials with ruthenium, a distilled water rinse was necessarily withheld until after heat treatment to ensure the stability of the mesopores and particle morphology. For all samples mentioned in this paper, calcination was done in an environment of air or in a reducing environment of N_2 with 10% H_2, both ramped at 10 °C /min to 400 °C, then held for 4 h, then allowed to cool at the natural cooling rate of the furnace under the same calcinations environment. Hereafter, the weight percent of ruthenium is reported relative to Ru+Nb metal content, irrespective of oxygen content. Sample names and associated treatments are summarized in Table 1.

2.4. Characterization of Metal Oxides. X-ray diffraction patterns (XRD) were collected with a Scintag PadV Gonniometer/Diffractometer, and data analysis, including Rietveld refinement, performed with Jade 8.0 software. X-ray photoelectron spectroscopy (XPS) analysis was performed on a Kratos Axis Ultra XPS with a monochromatic Al Kα source operated at 300 W. Data analysis quantification was performed using CasaXPS software. Thermogravimetric analysis (TGA) was performed on TA Instruments SDT Q600 TGA/DSC. High-resolution transmission electron micrographs (TEM) were obtained on a JEOL 2010 running at 200 kV, while scanning transmission electron micrographs (STEM) were obtained on a JEOL 2010 FEG TEM at 200 kV. Both microscopes are equipped with Oxford EDS units. Scanning electron microscopy (SEM) images were acquired using a Hitachi S-5200 SEM, also equipped with EDS. A Quantachrome Autosorb-1 was used to determine adsorption isotherms, estimate surface area, and obtain pore size distributions. Resistance measurements were made with an in-house device in which ~30 mg of material is weighed and compressed between positive and negative contact points to a consistent, estimated bulk density, whereas an Ohm meter, sensitive to ±0.01 Ω, measures resistance. Cyclic voltammograms were acquired on a Pine model AFCBP1 potentiostat. The measurements were made using a Pt gauze counter electrode and a mercury−mercury oxide (Hg/HgO) reference electrode. The potential of the reference electrode corresponds to +0.92 V vs RHE in 1 M KOH. A thin film of material was applied to the glassy carbon disk electrode from a solution containing electrocatalyst and Nafion. Here, nafion was not used as an active

Table 1. Summary of Post-Treatments and Resulting Material Properties of All Samples

sample ID	elemental content	wash step	heating step	BET (m^2/g)	resistance (Ω)	color
Vulcan XC-72	C, O			200−250	<0.01	black
RuO_2 (J&J Mtrls.)	Ru, O			122	0.4	black
Nb_2O_5 (HY340)	Nb, O			183	8.30×10^6	white
NbO_x-Dry-Air	Nb, O	omitted	air 10 °C/min 400 °C 4 h	2	6.60×10^6	white
NbO_x-Wash-Air	Nb, O	excess soln.	air 10 °C/min 400 °C 4 h	183	8.40×10^6	white
NbO_x-Dry-N_2/H_2	Nb, O	omitted	N_2/10 % H_2 10 °C/min 400 °C 4 h	2	8.10×10^6	black
NbO_x-Wash-N_2/H_2	Nb, O	excess soln.	N_2/10 % H_2 10 °C/min 400 °C 4 h	131	7.90×10^6	gray
$NbRu_yO_z$-Dry-Air	Nb, Ru, O	omitted	air 10 °C/min 400 °C 4 h	2	8.20×10^6	light green
$NbRu_yO_z$-Wash-Air	Nb, Ru, O	excess soln.	air 10 °C/min 400 °C 4 h	164	8.20×10^6	green
$NbRu_yO_z$-Dry- N_2/H_2	Nb, Ru, O	omitted	N_2/10 % H_2 10 °C/min 400 °C 4 h	10	<0.01	black
$NbRu_yO_z$-Wash-N_2/H_2	Nb, Ru, O	excess soln.	N_2/10 % H_2 10 °C/min 400 °C 4 h	80	950	black
$NbRu_yO_z$-Wet-N_2/H_2	Nb, Ru, O	wetted	N_2/10 % H_2 10 °C/min 400 °C 4 h	167	2.3	black

ion transport barrier, but merely as a binding agent. The loading of the catalyst on the glassy carbon working electrode was 128 $\mu g/cm^2$.

3. RESULTS

As-produced powders of niobium oxide and Ru-modified niobium oxide appeared visually indistinguishable in SEM as collected directly from the filter paper after spray pyrolysis at 200 °C. Collected particles were polydisperse, ranging from roughly 50 nm to 4 μm. SEM-EDS indicated Ru content in $NbRu_yO_z$ particles was in the range of 6−13 %, with an average just slightly below the nominal level of 12 wt % that was in the precursor mixture. Because spray pyrolysis involves very small particles at elevated temperatures, components with significant vapor pressures at the processing conditions can undergo evaporative loss, which can result in composition changes in multicomponent particles if one component is more volatile than another (20, 21). All samples mentioned hereafter originated from one of two parent samples as collected directly from the SP system, one a niobium oxide sample (NbO_x) and the other a Ru-modified niobium oxide ($NbRu_yO_z$). Sample names reflect the metal oxide(s) of the parent sample and the specific post-treatment received, as described further below.

3.1. Niobium Oxide Materials. NbO_x-Dry-Air was calcined in air at 10 °C/min to 400 °C for 4 h, without any acid washing step. A similar sample, NbO_x-Dry-N_2/H_2, received the same treatment with heating in an N_2/10 % H_2 atmosphere instead of air. BET measurements in both cases show a surface area of ∼2 m^2/g, with resistance readings equivalent to uncalcined Nb_2O_5. NbO_x-Dry-N_2/H_2 becomes a black powder, whereas its equivalent calcined in air remains white following heat treatment. In neither of these powders was the interior mesoporosity well-exposed (as indicated by the low surface areas), though interior mesochannels of size 5−6 nm in diameter were apparent by TEM (Figure 1A). The change of color to black when using the reducing calcination atmosphere in the NbO_x-Dry-N_2/H_2 treatment, perhaps combined with trapped organic material, appears to have at least partially reduced niobia during the treatment, and led to surface crystallization that is apparent from lattice fringes in TEM shown in Figure 1B. Analysis of these fringes (inset of Figure 1B) reveals reflections from (100) & (131)/(180) orthorhombic Nb_2O_5. XPS results (not included here) of NbO_x-Dry-N_2/H_2 indicated the presence of Nb(IV) on the surface of the material, which is consistent with the color change to black, but it is likely the bulk remains as Nb(V) based on the high electrical resistance (∼1 × 10^7 Ω), which is consistent with reported values for Nb_2O_5 (10, 26).

3.2. Mixed-Metal Oxides. The Ru-modified niobium oxide ($NbRu_yO_z$) was also synthesized without an acid washing step and with calcination in air at 400 °C for 4 h ($NbRu_yO_z$-Dry-Air). Close examination of the powders by SEM and EDS revealed that particles with diameters in the range of 800 nm to 1.5 μm were covered with what were apparently ruthenium oxide crystalline growths (Figure 1C). EDS of multiple such particles indicated an average ruthenium content of ∼31 wt % with a range of 18−80 %, much more than the expected amount, assuming $RuCl_3$ was homogeneously mixed in the precursor solution. $NbRu_yO_z$ particles produced with a calcination in N_2/10 % H_2 ($NbRu_yO_z$-Dry-N_2/H_2) did not display the surface crystallization features by TEM that were seen with nonruthenium containing particles under the same atmosphere. While all previous samples were electrically resistive, this material displayed no measurable resistance reading (<0.01 Ω), and had a BET surface area of 9.3 m^2/g. The relatively low surface area implies that much of the internal surface is still occluded, however enough of the material is apparently partially reduced to give the low resistance measurement and black color. Nevertheless, increased internal surface area is needed for a desirable support for an electrocatalyst such as Pt.

Despite the lack of an acid washing step to remove surfactant, the presence of ruthenium oxide surface crystals on the $NbRu_yO_z$-Dry-Air samples clearly indicates that Ru species are able to permeate from the particle interiors during thermal postprocessing. The ruthenium oxide surface deposition is apparently particle size dependent. In none of the Ru-modified samples produced do particles smaller than 260 nm have crystalline deposits on their surface, and EDS measurements on these particles indicates no significant Ru content. In contrast, particles that are roughly 800 nm in diameter and larger consistently exhibit these crystals forming on their surface. It is consistent with diffusion principles

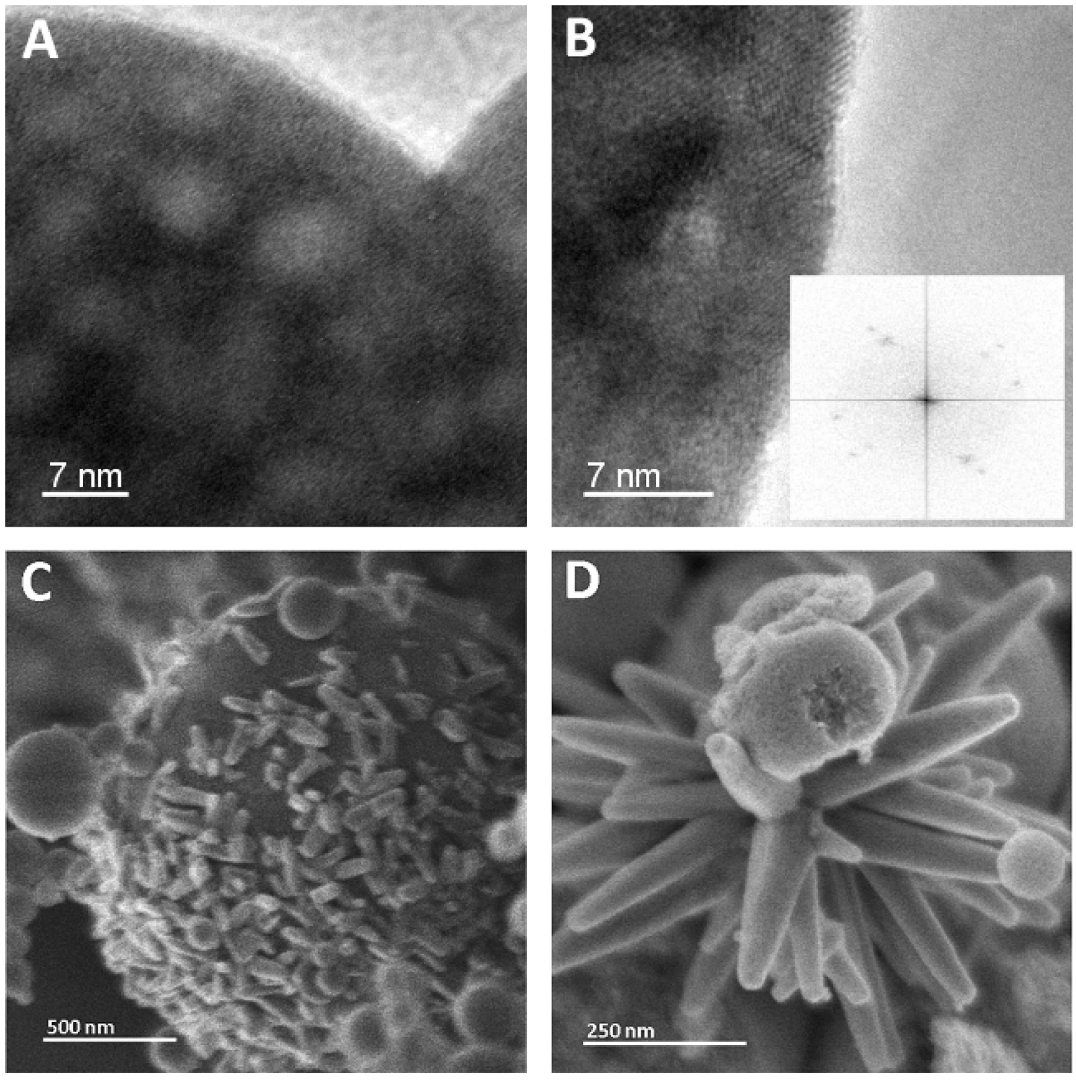

FIGURE 1. TEM showing (A) the 5−6 nm diameter mesopores of NbO_x-Dry-Air, and (B) lattice fringes of crystalline niobia formed in NbO_x-Dry-N_2/H_2. SEM of (C) $NbRu_yO_z$ calcined in air without a washing step ($NbRu_yO_z$-Dry-Air), and (D) with a washing step ($NbRu_yO_z$-Wash-Air).

that volatile Ru species would able to diffuse to and escape from smaller particles more quickly than from larger particles during calcination. Apparently, when the system begins to cool at the end of the calcination step, the environment around the smaller particles is too depleted in Ru species to be conducive to ruthenium oxide nucleation and growth. However, the larger particles do apparently have a sufficiently high concentration of Ru vapor species near the surface to lead to nucleation and growth during cooling. Nucleation of RuO_x on the larger particles surfaces could also be favored because of differences in surface composition. In addition, conditions are not homogeneous for particles at different locations inside the crucible during calcination/cooling, which could also contribute to our observations.

3.3. Mixed-Metal Oxides with Acid Wash Post-Treatment. With the introduction of an acid washing step before calcination in air at 400 °C for 4 h, $NbRu_yO_z$-Wash-Air showed very dramatic localized Ru oxide crystalline growths. We believe that etching of the particle surfaces by the acid wash opens up internal porosity, reduces transport resistance for volatile species, and promotes the rapid evaporative loss of Ru from particle interiors during calcination. During cooling vapor Ru species apparently nucleate and grow in favored locations.

When the $NbRu_yO_z$ is acid washed before calcination in a reducing atmosphere ($NbRu_yO_z$-Wash-N_2/H_2), the material was less, but still reasonably, conductive compared to $NbRu_yO_z$-Dry-N_2/H_2, with a resistance of 950 Ohm, and had a much improved BET surface area of 80 m^2/g. EDS showed a reduced ruthenium content of ~6% (average over multiple particles), indicating some Ru loss relative to the solution composition, but much less loss than the $NbRu_yO_z$-Wash-Air material. Compared with the BET of mesoporous NbO_x-Wash-Air, there is a reduction of ~100 m^2/g in surface area, the reason for which is not completely clear, but it apparently related to interaction of the acid wash with the $NbRu_yO_z$ material.

3.4. Optimized Mixed-Metal Oxide Support. The initial intent of the acid wash step was to etch oxide and surfactant in the outermost, lamellar surface layers, opening up internal surface area and allowing better penetration of the reducing N_2/H_2 atmosphere into the particle interior without extensive degradation of the interior structure. On the basis of this objective, and the observation of significant

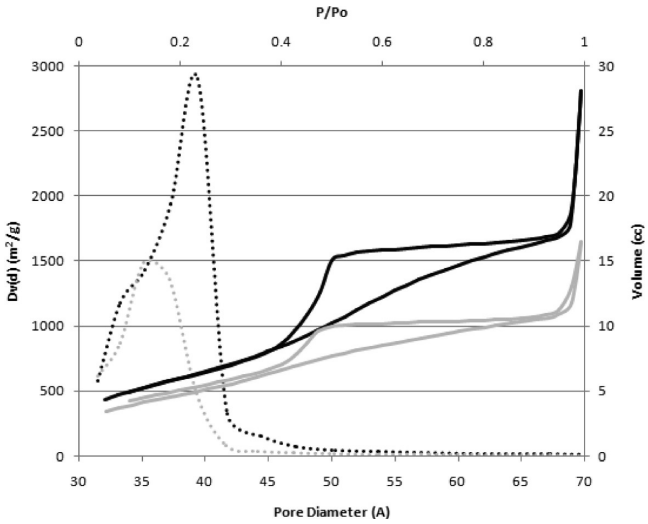

FIGURE 2. Adsorption−desorption isotherms in N_2 (solid, top and right axes) and corresponding pore size distributions calculated by the BJH method (dotted, bottom and left axes) for NbO_x-Wash-Air (dark) and $NbRu_yO_z$-Wet-N_2/H_2 (light).

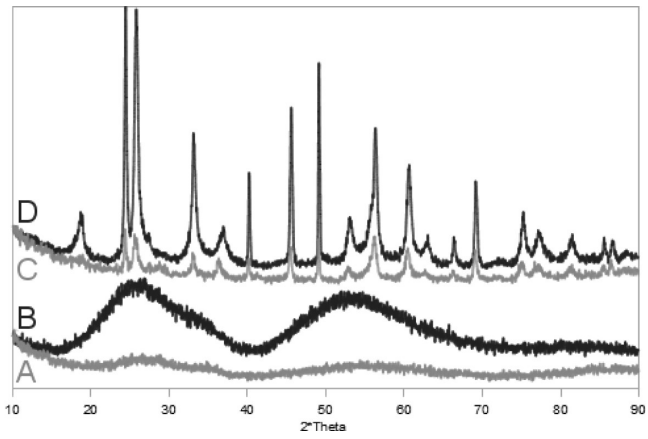

FIGURE 3. X-ray diffraction patterns from 10 to 90° 2θ for (A) $NbRu_yO_z$-Wet-N_2/H_2 and (B) NbO_x-Wash-Air, as well as (C, D) both samples after additional heating at 900 °C for 5 h in N_2, respectively.

surface area loss using the acid wash procedure, we tested a new etching procedure that utilized much less acid. With this treatment, $NbRu_yO_z$ was wet by dropwise addition of 0.3 M H_2SO_4 acid solution onto the powder inside a ceramic boat until all areas were wetted while maintaining the powder's original green color. The excessive acid addition associated with the "wash" step in the $NbRu_yO_z$-Wash-N_2/H_2 material led to a change in color from green to black before calcination, which is indicative of a change in oxidation state of the powder surface. The remaining inhibition to diffusion after the wetting procedure was apparently enough to limit significant Ru volatilization and surface area loss. After the reductive calcination, the resistance of $NbRu_yO_z$-Wet-N_2/H_2 was 2.3 Ohm, with a BET of 167 m^2/g and ~12 wt % Ru content as detected with EDS (average of multiple particles). This represented the most optimal combination of properties among powders synthesis and processing that were assessed in this work.

3.5. Adsorption Isotherms: Porous Structure of Supports. Selected full N_2 adsorption−desorption isotherms were conducted to better characterize the differences in pore structure between NbO_x and $NbRu_yO_z$ powders. The pure niobia (NbO_x-Wash-Air) sample had a pore size distribution centered around 3.9 nm while the niobia/ruthenia sample ($NbRu_yO_z$-Wet-N_2/H_2) was at 3.6 nm (Figure 2). Both values are similar to that of commercially available HY-340 (Nb_2O_5, CBMM) with a mesopore diameter of 3.8 nm. Calcination has typically been shown in the literature to cause pores to grow in size (23), which could uniquely alter the pore size distribution of different materials depending upon how they respond to thermal treatment. Despite the difference in pore size distributions, surface areas were very comparable at 183 and 167 m^2/g for niobia and niobia/ruthenia samples, respectively. Both samples exhibited significant hysteresis of type H1/H2 according to the IUPAC model, common for mesoporous oxides (16, 18, 22, 24). Such hysteresis behavior is often indicative of pores that are necked or have restricted access. These results show that both samples are very similar structure. The observed hysteretic pore volumes were 13 and 11% for the niobia and ruthenium-modified niobia, respectively. Interestingly, the adsorption and desorption curves of $NbRu_yO_z$-Wet-N_2/H_2 do not merge at low pressures. This repeatable result is not fully understood, but could be due to swelling of the mesostructure during adsorption, which further exposes interior porosity that was previously inaccessible. Hysteresis then results during desorption when some N_2 is trapped within these pores.

3.6. X-ray Diffraction Spectroscopy (XRD): Phase Structure of Supports. XRD was performed to determine crystalline phase development in selected powders. Patterns A and B in Figure 3 show XRD patterns for $NbRu_yO_z$-Wet-N_2/H_2 and NbO_x-Wash-Air. Both powders displayed poorly developed crystallinity, with no distinct crystalline phase evident after calcination. However, the niobia powder had two clear broad peaks, indicating the onset of order, whereas the $NbRu_yO_z$ sample appeared essentially completely amorphous. Both spectra are comparable to that attained by others (14, 18) for material containing only Nb(V), though these data are insufficient to conclude phase or oxidation state. The incorporation of ruthenium in our materials appears to delay the onset of niobia crystallization, an effect that is common for substituted or doped oxides. It can be concluded that the superior electrical conductivity of $NbRu_yO_z$-Wet-N_2/H_2 is not due to substantial crystallization or crystalline phase content because the bulk of both samples was mostly amorphous.

Additional heating of these samples at 900 °C for 5 h in N_2 (Figure 3C and 3D) did lead to the development of well-defined crystalline patterns. This is not surprising since crystallization of Nb_2O_5 into an orthorhombic structure is known to begin around 500 °C (19, 27, 28). This is eventually followed by an irreversible transition to a monoclinic crystal state at ~900−1000 °C (14, 27). The peaks for both powders were identically located with similar peak widths; however, the peaks for $NbRu_yO_z$ were significantly lower in intensity. This indicates that, after heating to 900 °C, the crystalline phase content of $NbRu_yO_z$ is apparently the same

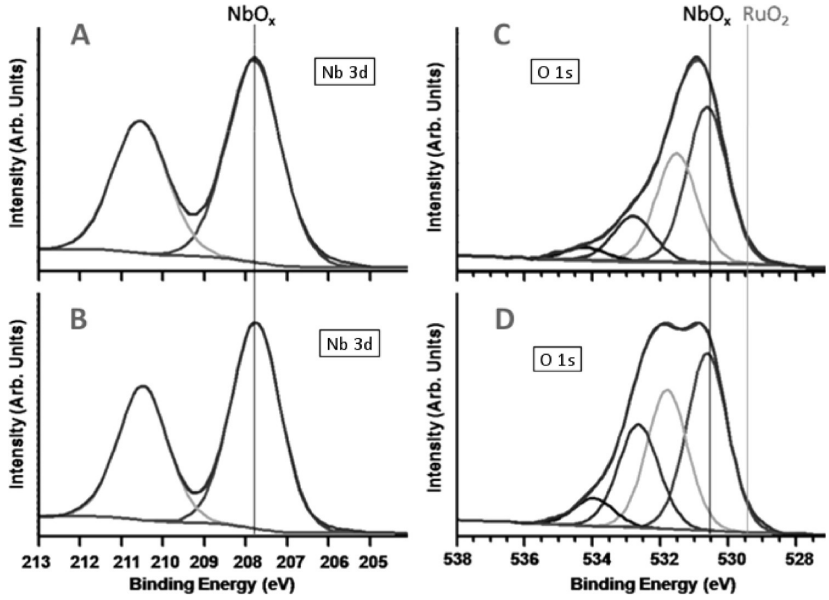

FIGURE 4. High-resolution XPS spectra: (A) Nb 3d spectrum of $NbRu_yO_z$-Wet-N_2/H_2, (B) Nb 3d spectrum of NbO_x-Wash-Air, (C) O 1s spectrum of $NbRu_yO_z$-Wet-N_2/H_2, and (D) O 1s spectrum of NbO_x-Wash-Air.

as in pure NbO_x; however, the relative amount of crystalline material is less. We were not able to index the peaks in C and D to known spectra of Nb(V), Nb(IV), or Nb(II) from the JCPDS database. However, a variety of substoichimetric oxides exist for niobia-based materials that are highly dependent upon the method and conditions of preparation (14, 27, 29). In fact, the peaks observed in (C)/(D) are very similar to diffraction patterns published recently for single-crystal (30, 31) and powder (27) $Nb_{12}O_{29}$ and $Nb_{22}O_{54}$.

3.7. X-ray Photoelectron Spectroscopy (XPS): Surface Chemistry Studies. XPS high-resolution Ru 3d, Nb 3d, and O 1s spectra were also acquired from the NbO_x-Wash-Air and $NbRu_yO_z$-Wet-N_2/H_2 powders to provide oxidation state information. The Nb3d spectrum acquired from both materials corresponded well to the Nb_2O_5 phase (Figure 4B). The shape and position of Nb 3d spectra acquired from the $NbRu_yO_z$ material (Figure 4A) is very similar to that of NbO_x, indicating that the oxidation states of surface niobium in each are similar. O 1s spectra and their curve-fits are shown in panels C and D in Figure 4. In the O 1s spectrum of the NbO_x material, the main peak is positioned at 530.6 eV and can be assigned to oxygen-bound to niobium in Nb_2O_5. The peak at 531.6 eV can be attributed to surface OH^- species. The last two components, at 532.8 and 534 eV can be assigned to adsorbed H_2O and/or CO and CO_2 species. The O 1s spectrum of the $NbRu_yO_z$ material contains the same 4 peaks as that of the NbO_x material. The main difference between the two materials is the amount of oxygen associated with OH−, adsorbed H_2O and/or CO and CO_2. The post reductive treatment of the material at elevated temperature in a N_2/H_2 atmosphere appears to result in a decrease in these species as compared to the post-treatment in air.

Interestingly, the peak indicative of ruthenium oxide phase at lower binding energies is not present. Another source of information regarding the oxidation state of ruthenium can be obtained from the Ru 3d spectrum.

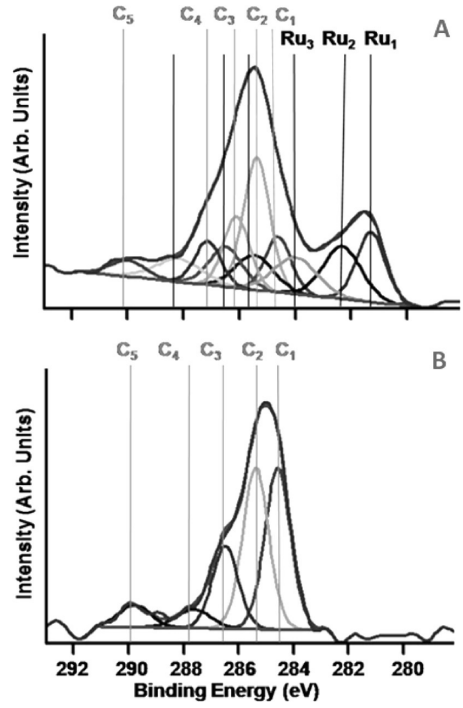

FIGURE 5. High-resolution Ru 3d and C 1s XPS spectra of (A) $NbRu_yO_z$-Wet-N_2/H_2 and (B) NbO_x-Wash-Air.

However, this is not straightforward because the binding energies (BE) of ruthenium and carbon species are in the same window. A high-resolution Ru 3d XPS spectrum acquired from these materials is shown in Figure 5. Ru 3d spectra have 2 spin−orbit components corresponding to the Ru $3d_{5/2}$ (lower BE side of Ru 3d) and Ru $3d_{3/2}$ (higher BE side). The separation between these components is 4.2 eV. Three doublet peaks in the Ru 3d spectrum correspond to ruthenium components and 5 peaks correspond to carbon components. The carbon components present in the $NbRu_yO_z$ material spectrum strongly coincide with carbon components present in the C 1s spectrum of the NbO_x material

(Figure 5B), which does not have contributions from ruthenium. Typically, the BE of 5/2 component of metallic ruthenium lies in the 279.8−280.2 eV range and that of ruthenium in RuO_2 is in the range 280.5−281.0 eV. The first ruthenium component in the Ru 3d spectrum of the $NbRu_yO_z$ material is at 281.3 eV, which is significantly higher than expected for metallic ruthenium and slightly higher than expected for RuO_2. This peak also cannot be assigned to a higher oxidation state. The second ruthenium peak in Ru 3d spectrum is around 282.3 eV, and can be assigned to hydrous ruthenium(IV) oxide. The third peak is around 284 eV and is attributed to RuO_4.

The absence of the RuO_2 peak in the O 1s spectrum, as well as the slightly higher than expected BE of the first ruthenium peak for RuO_2, can be explained by the formation of a mixed Nb−Ru oxide phase. It is possible that incorporation of Ru(IV) into the Nb_2O_5 phase results in a shift of ruthenium BE to higher values, while the BE of oxygen bonded to ruthenium becomes indistinguishable from that of oxygen bound to niobium. Another observation that supports incorporation of ruthenium oxide into the niobium oxide matrix is the ratio of oxygen bound to niobium (from O1s spectrum) to niobium. In the NbO_x material O_{Nb2O5}/Nb_{Nb2O5} is around 2.7, which is very close to the stoichiometry of Nb_2O_5. In comparison, the same ratio in the $NbRu_yO_z$ material is around 1.9, and would be even lower were ruthenium content also considered. This means that the average number of oxygen atoms per metal atom in the $NbRu_yO_z$ material is close to the stoichiometry of IV valency metal oxides.

3.8. Thermogravimetric Analysis of Metal Oxides. Thermogravimetric analysis was performed to mimic the entire post-treatment process of NbO_x-Wash-Air and $NbRu_yO_z$-Wet-N_2/H_2 to better understand the extent to which incompletely reacted precursors or impurities exist that may influence the powder properties, as well as to observe oxidation−reduction behaviors of the materials. After heating of the as-produced SP powders at 400 °C for 4 h in their respective atmospheres in the TGA, both samples were then ramped at 10 °C/min to 1500 °C in a N_2 atmosphere (Figures 6A and 6B). Weight decrease from 20−400 °C can be attributed to loss of residual water and alcohol within the mesopores of the material, as well as much of the original surfactant. The rate of loss in $NbRu_yO_z$-Wet-N_2/H_2 is equivalent to that of NbO_x-Wash-Air, though delayed by roughly 60 °C until ∼245 °C when the rate of loss from NbO_x-Wash-Air decreases. This is possible because much of the ruthenium content is in the form of hydrous RuO_2, wherein water remains stable slightly longer (1, 3). The difference in weight loss profiles A and B in Figure 6 seen from 0 to 50 min could be attributed to differences in the mobility of volatile species within each material, in combination with different rates of loss associated with particles of various sizes within the poly dispersed bulk. Complete dehydration may continue to 400 °C and perhaps beyond, and loss of P123 surfactant is expected to begin around 200 °C and finish within the 4 h period held at 400 °C. Throughout this holding period, both samples decrease equally in weight (47.9% loss for A and 47.3% loss for B), indicating that the different calcination atmospheres do not substantially affect the degree to which volatile species are removed from the materials.

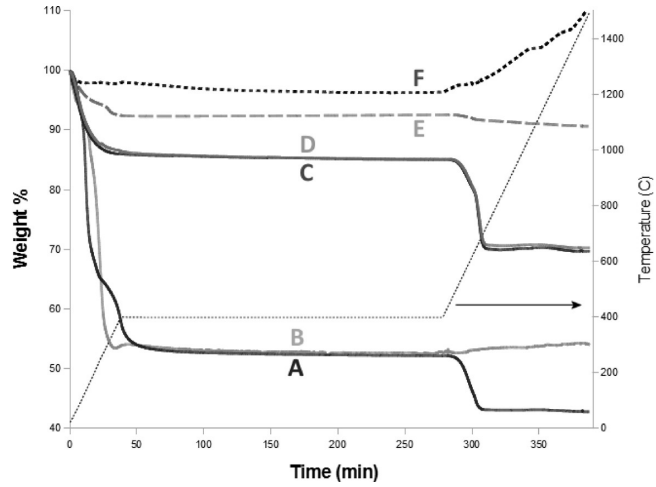

FIGURE 6. Thermogravimetric analysis of NbO_x-Wash and $NbRu_yO_z$-Wet under the same conditions experienced during post-treatment. Samples were ramped at 10 °C /min to 400 °C in their respective atmospheres, where they were held for 4 h. All samples were then exposed to a N_2 atmosphere during heating from 400 to 1500 °C at the same ramp rate. At temperatures of 400 °C and below, (A) NbO_x-Wash was in air, (B) $NbRu_yO_z$ was in N_2/10%H_2, (C) previously post-treated NbO_x-Wash-Air was in air and (D) N_2/10%H_2, and (E) previously post-treated $NbRu_yO_z$-Wash-N_2/H_2 and (F) $NbRu_yO_z$-Wet-N_2/H_2 were both in N_2.

Previously calcined samples of NbO_x-Wash-Air underwent the same temperature program in air (Figure 6C) and N_2 (Figure 6D). Both samples initially lost 14% of their weight, accounting for adsorbed water during their exposure to the atmosphere as collected powders. Furthermore, both samples had nearly identical weight loss profiles at all temperatures, indicating little difference between these two atmospheres for volatiles removal or oxidation state changes. Similarly, $NbRu_yO_z$-Wash-N_2/H_2 (Figure 6E) and $NbRu_yO_z$-Wet-N_2/H_2 (Figure 6F) were heated under the same conditions as the samples in plots C and D in Figure 6. The $NbRu_yO_z$ samples displayed less weight loss below 400 °C than the NbO_x samples, indicating less residual water and alcohol. However, much more notable is the distinctly different behavior of the $NbRu_yO_z$ and NbO_x samples above 400 °C. All NbO_x samples in Figure 6 show an abrupt weight loss of roughly 17 wt % beginning at approximately 450 °C, whereas all $NbRu_yO_z$ samples show only a small weight decrease or a weight increase above 400 °C. The NbO_x behavior is not yet fully understood; however, it seems likely that it may be related to the onset of crystallization since a series of crystalline phase transitions for niobia is reported to initiate at ∼500 °C (27). The behavior of the $NbRu_yO_z$ samples above 400 °C is likely related to slight changes in oxidation state related to the change in gas atmosphere at and above 400 °C, possibly coupled with the effect of temperature on residual volatiles or oxidation state. The sizable weight increase of $NbRu_yO_z$-Wet-N_2/H_2 (Figure 6F) is noteworthy, and supports the notion that this sample is

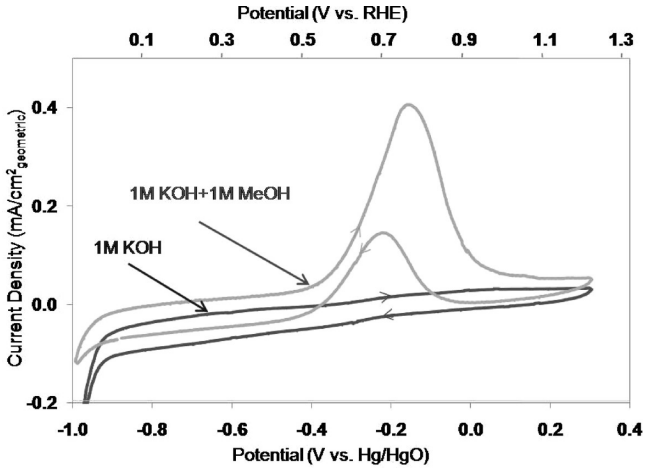

FIGURE 7. Cyclic voltammagrams of 128 μg/cm^2 $NbRu_yO_z$-Wet-N_2/H_2 initially in 1 M KOH solution, and then with 1 M methanol added. Scan rate of 10 mV/s vs Hg/HgO reference electrode.

more reduced than the other samples, which is consistent with the low resistance of that powder.

3.9. Electrochemical Characterization of Electrocatalysts and Catalyst Supports. Based on superior surface area and low electrical resistance, the $NbRu_yO_z$-Wet-N_2/H_2 material was judged to have the best potential as a viable electrocatalyst support. That material was therefore selected for electrochemical characterization. Cyclic voltammetry in Ar-saturated 1 M KOH was used to address the feasibility of using $NbRu_yO_z$ produced by spray pyrolysis as a support for anode catalysts in fuel cells. Within the given range of potential of the cyclic voltammogram shown in Figure 7, there are no pronounced features until H_2 evolution at about −0.9 V. This indicates an absence of anion or cation adsorption on the electrode. Upon addition of methanol, the oxidative process indicates oxidation of the alcohol on the $NbRu_yO_z$ material. This shows that, unlike carbon, this $NbRu_yO_z$ support material does have some activity for the process of fuel oxidation. The onset of the oxidation process is expected to improve once platinum catalyst is incorporated on the support material.

4. DISCUSSION

The changes experienced by a particle during the pyrolysis and post-treatment of metal-oxides are depicted in the illustration of Figure 8. Part of the significance of this study is derived from the control that is possible with this process. Aerosolization produces homogeneous liquid droplets of the same composition as the precursor solution. Evaporation of solvents from the droplets then proceeds (A), leading to solute precipitation. Because solvent evaporation occurs from the droplet surface, solute concentration gradients develop inside droplets that typically results in precipitate or solid formation first at the droplet surface (B). For the same reason, during EISA in evaporating droplets, concentration gradients of the surfactant (P123) will develop that trigger the surfactant liquid crystalline (LC) phase transformations, usually first at the surface of the droplet. Continued solvent evaporation leads to the propagation of surfactant LC transitions into the interior of the droplet. Because of the very short evaporation times of submicrometer droplets, much of this may happen even before droplets enter the furnace zone. The higher temperatures of the heated zone complete solvent evaporation, and drive decomposition of the precursor compounds, effectively locking in any surfactant-related mesostructure that has developed. The LC mesostructural phases that form depend on the particular phase behavior of the surfactant, and the concentrations that develop during solvent evaporation. For the case of P123 under the conditions employed here, electron microscopy indicates that a lamellar phase often forms at the surface first (C), followed by a wormlike or hexagonal mesophase in the interior of particles (C and D in Figure 9). As this work shows, if the collected powder receives the proper post-treatment, the process yields particles with fully exposed, mesoporous interiors (F).

TEM micrographs C and D in Figure 9 are representative of the structure depicted in illustration (E) of Figure 8: $NbRu_yO_z$ particles collected directly from the filter paper show a visible mesoporous interior isolated by 2−3 lamellar layers at the surface. Those layers apparently collapse upon removal of their surfactant scaffolding and partially sinter when this material is calcined in air, as do the structural walls of the interior, resulting in larger, more visually distinct pores (Figure 9A). Interior surface area may not be fully accessible and residual organic material from any remaining surfactant may be kinetically trapped within particles under these conditions. Larger particles sometimes rupture, apparently due to interior pressure buildup associated with restrictions on the escape of volatiles (Figure 10). After acid etching, the lamellar surface layer appears to be gone (Figure 9B), and calcination effectively removes organics and opens up internal surface area, as supported by the TGA results and surface area measurements reported.

Because of the submicrometer droplet and particle sizes in aerosol pyrolysis, and the nanoscopic dimensions of the pore structures, multicomponent aerosol-derived materials such as these can be very sensitive to evaporative loss of

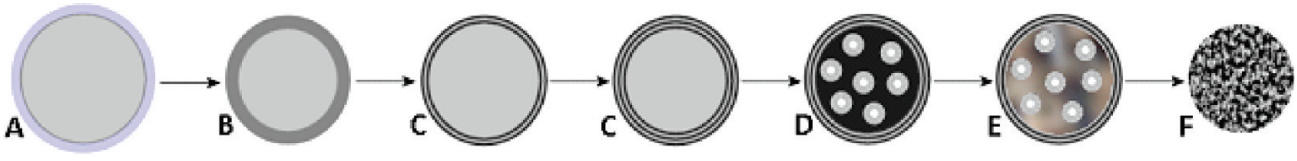

FIGURE 8. Schematic depiction of transformations that occur during spray pyrolysis of Nb/Ru precursor solution containing a surfactant template, followed by post-treatment. (A) Evaporation begins as a vapor layer forms around the droplet. (B) Precipitation of the outer surface. (C) Outer layers begins to dry faster than interior moisture diffuses to the surface, resulting in formation of vesicles from surfactant. (D) Entire droplet eventually dries. (E) Thermolysis of chloride precursors into porous metal oxides. (F) Proper post-treatment exposes the intact mesoporous structure.

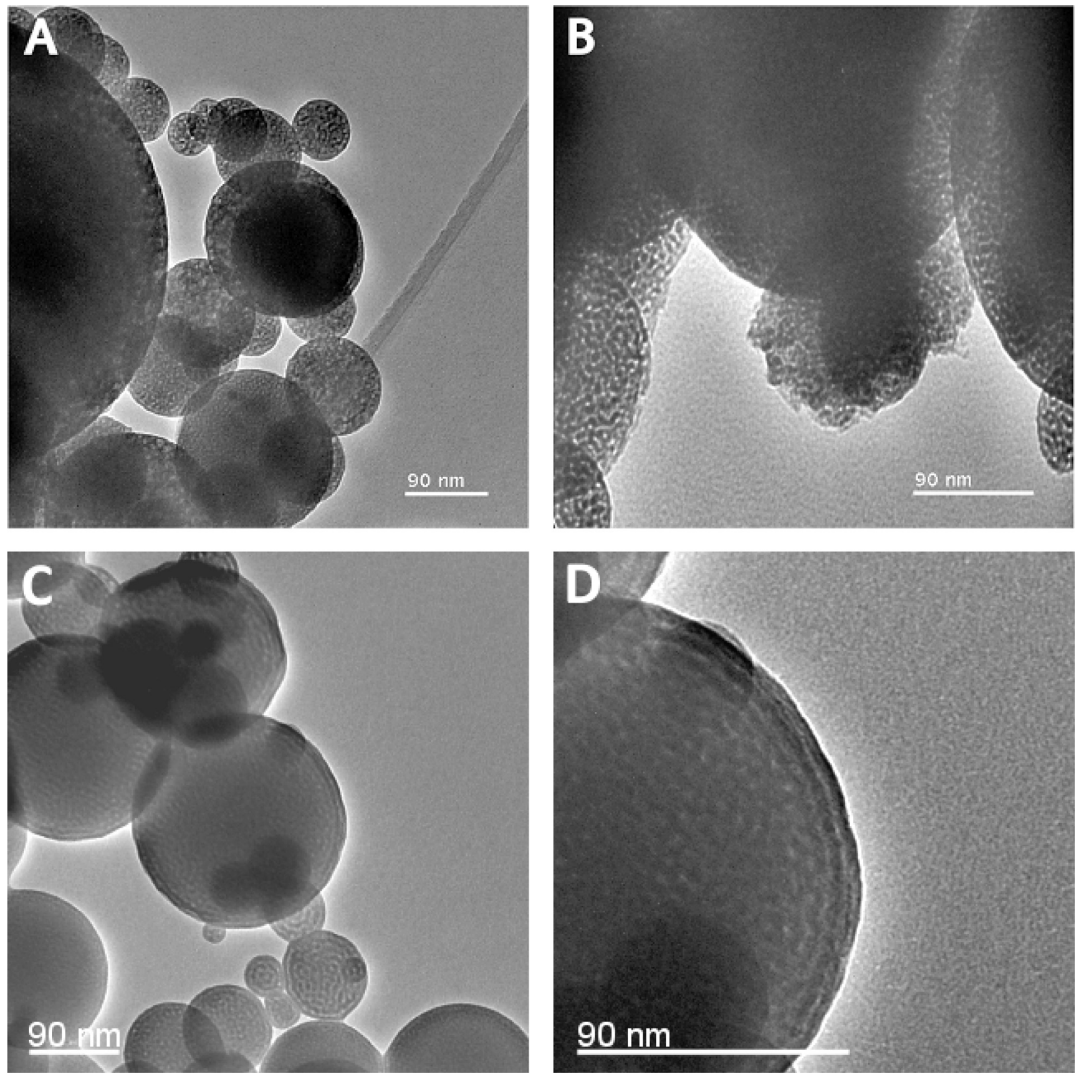

FIGURE 9. TEM of (A) $NbRu_yO_z$-Dry-Air (calcined without a washing step), and (B) STEM of $NbRu_yO_z$-Wet-N_2/H_2 (calcined with a preceding acid washing step). (C) $NbRu_yO_z$ particles of various sizes before any post-treatment, showing a 3D wormhole porous structure in the particle interior and 2−3 exterior lamellar layers. (D) Higher-magnification clarifies the separate structures.

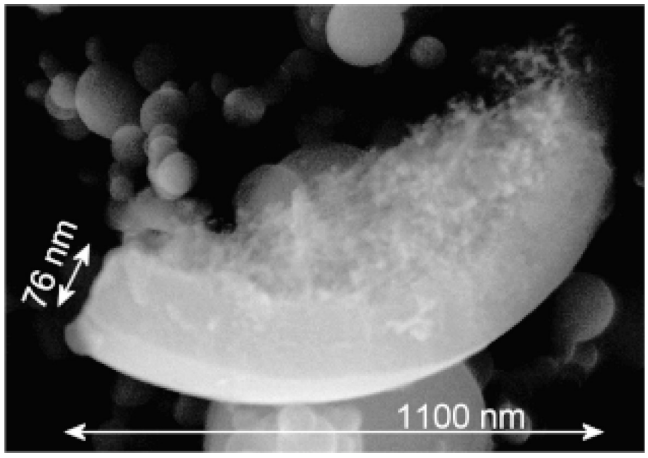

FIGURE 10. SEM image of a particle fragment of $NbRu_yO_z$-Dry-Air. During spray pyrolysis or thermal processing, particle surfaces may become nearly impermeable before volatile species can escape to the atmosphere. The pressure developed by these trapped volatiles is sometimes sufficient to fracture some particles.

species that have a significant vapor pressure at the processing conditions. Preferential evaporative loss of one element can lead to compositional deviations within the parent particles, and the volatilized material may migrate and end up elsewhere as a coating or distinct phase. Relevant to this work, it has been reported that ruthenium species possess a significantly lower energy of vaporization compared to niobium (32, 33). This is consistent with the observations in this work of Ru depletion in powders calcined at 400 °C, though as-produced powders made at 200 °C did not have substantial Ru depletion.

5. CONCLUSIONS

Spray pyrolysis of ethanolic solutions of chloride precursors was used to synthesize polydisperse (20 nm−1.6 μm), mesoporous niobium oxide, and ruthenium-modified niobium oxide. Evaporation-induced self-assembly of the pluronic surfactant P123 led to poorly ordered mesoporous particles with BET surface areas as high as ~180 m^2/g, and pore diameters in the 3.5−4 nm range. An acid etching treatment was needed to open up internal surface area, and several variations of postprocessing involving acid washing

and heating under different atmospheres have been explored. The final morphological, compositional, and electrical properties of the end product have been reported relative to manipulation of these post-treatments. Most notably, acid wetting of powders produced from a Nb/12 wt % Ru precursor mixture, followed by reduction in N_2/10% H_2 at 400 °C, resulted in a promising material that possessed 167 m^2/g surface area and had low electrical resistance (2.3 Ω). This material, which apparently consists of Ru integrated into the niobium oxide matrix, was also tested for electrochemical behavior and found to have activity for the oxidation of methanol in the absence of platinum catalyst. The intrinsic properties of this $NbRu_yO_z$ material suggest that it can be utilized in fuel cells as a reactive support for electrocatalyst. The synthesis of Pt/$NbRu_yO_z$ materials and the investigation of their cocatalysis properties are currently being explored.

Acknowledgment. This work was supported by the DoE-EPSCoR New Mexico Implementation Program: Materials for Energy Conversion, DOE-EERE Advanced Cathode Catalysts Program (subcontract to Los Alamos National Laboratory), and the NSF though an IGERT Fellowship to D.K.

Note Added after ASAP Publication. In the version of this paper published to the Web on December 16, 2009, there were errors in the compound names in the Figure 1 caption and an incorrect electrical resistance value in section 3.1. The corrected version was published on December 18, 2009.

Supporting Information Available: Energy-dispersive spectroscopy (EDS) spectra supporting the approximate elemental metal compositions cited in the text (PDF). This material is available free of charge via the Internet at http://pubs.acs.org.

REFERENCES AND NOTES

(1) Pylypenko, S.; Blizanac, B. B.; Olson, T. S.; Konopka, D.; Atanassov, P. *ACS Appl. Mater. Interfaces* **2009**, *1*, 604–611.
(2) Sasaki, K.; Adzic, R. R. *J. Electrochem. Soc.* **2008**, *155*, B180–B186.
(3) Rolison, D. R.; Hagans, P. L.; Swider, K. E.; Long, J. W. *Langmuir* **1999**, *15*, 774–779.
(4) Borup, R.; Meyers, J.; Pivovar, B.; Kim, Y. S.; Mukundan, R.; Garland, N.; Myers, D.; Wilson, M.; Garzon, F.; Wood, D.; Zelenay, P.; More, K.; Stroh, K.; Zawodzinski, T.; Boncella, J.; McGrath, J. E.; Inaba, M.; Miyatake, K.; Hori, M.; Ota, K.; Ogumi, Z.; Miyata, S.; Nishikata, A.; Siroma, Z.; Uchimoto, Y.; Yasuda, K.; Kimijima, K. I.; Iwashita, N. *Chem. Rev.* **2007**, *107*, 3904–3951.
(5) Kinoshita, K. *Carbon—Electrochemical and Physicochemical Properties*; John Wiley & Sons: New York, 1988.
(6) Mayrhofer, K. J. J.; Ashton, S. J.; Meier, J. C.; Wiberg, G. K. H. *J. Power Sources* **2008**, *185*, 734–739.
(7) Bi, W.; Fuller, T. F. *J. Electrochem. Soc.* **2008**, *155*, B215–B221.
(8) Colon-Mercado, H. R.; Popov, B. N. *J. Power Sources* **2005**, *155*, 253–263.
(9) Antolini, E.; Gonzalez, R. R. *Solid State Ionics* **2009**, *180*, 746–763.
(10) Vettraino, M.; Trudeau, M.; Antonelli, D. M. *Inorg. Chem.* **2001**, *40*, 2088–2095.
(11) Garcia, B. L.; Fuentes, R.; Weidner, J. W. *Electrochem. Solid-State Lett.* **2007**, *10*, B108–B110.
(12) Park, K. W.; Seol, K. S. *Electrochem. Commun.* **2007**, *9*, 2256–2260.
(13) Sasaki, K.; Zhang, L.; Adzic, R. R. *Phys. Chem. Chem. Phys.* **2008**, *10*, 159–167.
(14) Bansal, N. P. *J. Mater. Sci.* **1994**, *29*, 4481–4486.
(15) Guerrero, S.; Miller, J.; Wolf, E. E. *Appl. Catal., A* **2007**, *328*, 27–34.
(16) Yuan, L.; Guliants, V. V. *J. Mater. Sci.* **2008**, *43*, 6278–6284.
(17) Brinker, C. J.; Lu, Y. F.; Sellinger, A.; Fan, H. Y. *Adv. Mater.* **1999**, *11*, 579.
(18) Yang, P. D.; Zhao, D. Y.; Margolese, D. I.; Chmelka, B. F.; Stucky, G. D. *Chem. Mater.* **1999**, *11*, 2813–2826.
(19) Romero, R.; Ramos-Barrado, J. R.; Martin, F.; Leinen, D. *Surf. Interface Anal.* **2004**, *36*, 888–891.
(20) Senzaki, Y.; Hampdensmith, M. J.; Kodas, T. T.; Hussler, J. W. *J. Am. Ceram. Soc.* **1995**, *78*, 2977–2983.
(21) Messing, G. L.; Zhang, S. C.; Jayanthi, G. V. *J. Am. Ceram. Soc.* **1993**, *76*, 2707–2726.
(22) Lee, B.; Lu, D. L.; Kondo, J. N.; Domen, K. *J. Am. Chem. Soc.* **2002**, *124*, 11256–11257.
(23) Lee, B.; Yamashita, T.; Lu, D. L.; Kondo, J. N.; Domen, K. *Chem. Mater.* **2002**, *14*, 867–875.
(24) Kondo, J. N.; Takahara, Y.; Lee, B.; Lu, D. L.; Domen, K. *Top. Catal.* **2002**, *19*, 171–177.
(25) Antonelli, D. M.; Nakahira, A.; Ying, J. Y. *Inorg. Chem.* **1996**, *35*, 3126–3136.
(26) Skadtchenko, B. O.; Antonelli, D. M. *Can. J. Chem.* **2006**, *84*, 371–383.
(27) Brayner, R.; Bozon-Verduraz, F. *Phys. Chem. Chem. Phys.* **2003**, *5*, 1457–1466.
(28) Lenzmann, F.; Shklover, V.; Brooks, K.; Gratzel, M. *J. Sol—Gel Sci. Technol.* **2000**, *19*, 175–180.
(29) Jehng, J. M.; Wachs, I. E. *Chem. Mater.* **1991**, *3*, 100–107.
(30) McQueen, T.; Xu, Q.; Andersen, E. N.; Zandbergen, H. W.; Cava, R. J. *J. Solid State Chem.* **2007**, *180*, 2864–2870.
(31) Waldron, J. E. L.; Green, M. A.; Neumann, D. A. *J. Phys. Chem. Solids* **2004**, *65*, 79–86.
(32) Jaksic, J. M.; Lacnjevac, C. M.; Krstajic, N. V.; Jaksic, M. M. *Chem. Ind. Chem. Eng. Q.* **2008**, *14*, 119–136.
(33) Massalski, T. B.; Okamoto, H. *Binary Alloy Phase Diagrams*; ASM International: Materials Park, OH, 1990.

AM900601Q